GSA DATA REPOSITORY 2012186

SUPPLEMENTARY MATERIAL

Northern Hemisphere forcing of the last deglaciation in southern Patagonia

Daniel S. Murray, Anders E. Carlson*, Brad S. Singer, Faron S. Anslow, Feng He, Marc Caffee, Shaun A. Marcott, Zhengyu Liu, Bette L. Otto-Bliesner
*Corresponding author: acarlson@geology.wisc.edu, 608-262-1921

Geologic Setting

Glacial deposits in the southern Patagonia region were first delineated in the mapping work of Caldenius (1932); further details regarding this area in later studies relied mainly upon minimally limiting radiocarbon dates (Mercer, 1976; Wenzens, 1999). Rio Guanaco Valley is centered upon 50°S in Argentine Patagonia. Elevation in this area ranges from ~650 to 800 m above sea level, while the adjacent Lago Viedma and Lago Argentino outlet valley lakes directly drain the Southern Patagonian Icefield and have much lower surface elevations than the valley floor elevations in Rio Guanaco Valley (Figs. 1 and DR1). Glacial activity in this area is not linked directly to the Southern Patagonian Icefield, but glacier growth and retreat for both ice masses should respond to the same climate changes. There are numerous well-preserved moraines in both the main valley and in the surrounding tributary valleys in this area (Wenzens, 1999) (Fig. DR1). For this study, boulder samples were collected for cosmogenic radionuclide surface exposure dating from two glacial features in Rio Guanaco Valley, namely the La Sofia and San Jorge moraines, which are the local last glacial maximum moraines in the valley. Another set of samples was collected from the smaller Cerro Pintado moraine located in the Rio Manga Norte Valley tributary valley north of Rio Guanaco Valley (Fig. DR1). Sample locations are shown in Figure 1b.

Cosmogenic Dating Methods

Exposure ages were derived by measurement of the *in situ* concentration of ^{10}Be within boulder surfaces from valley glacier moraines, accounting for the neutron and muon components of radionuclide production (Gosse and Phillips, 2001; Balco et al., 2008). A total of twenty-one samples were collected; all samples in this study have rhyolitic lithology. Six to nine samples were collected from each moraine, with coordinates recorded by GPS in the field (Table DR1). Boulder samples were chosen based on a preferred height (>1.0 m) to minimize the effects of shielding from topography or vegetation. All boulder faces were flat (<5° dip) and free from evidence of ventifaction. Samples were collected with hammer and chisel, while thicknesses were measured to account for the attenuation of cosmogenic ^{10}Be concentration with depth (Gosse and Phillips, 2001). Sampled boulders were clast-supported in order to lessen the likelihood that post-depositional exhumation had occurred (Gosse and Phillips, 2001; Balco, 2011). Representative samples are shown in Figures DR3–DR9.

Sample processing was performed in the Cosmogenic Radionuclide Laboratory facilities at the University of Wisconsin-Madison's Department of Geoscience. Each sample was first

crushed and separated into the 425-841 μm grain-size fraction range, rinsed, and then etched through repeated applications of HCl and HF acids until only quartz remained. Sample quartz purity was ensured by ICP-OES elemental analysis at the University of Colorado-Boulder. A procedural blank was made for each sample set in order to replicate all processing steps and potential contamination sources to which each sample may have been exposed. Five samples were processed in 2004 with blanks BL7 and BL8 (both with a $^{10}Be/^{9}Be$ ratio of $\sim 2.64\times10^{-14}$). The remaining sample sets were processed in 2010 with blanks B6 ($^{10}Be/^{9}Be=2.89\times10^{-15}$), B8 ($^{10}Be/^{9}Be=0.85\times10^{-15}$) and B9 ($^{10}Be/^{9}Be=1.25\times10^{-15}$). The UW-Madison laboratory has improved the process blank values via lowering the isotope ratios by more than one order of magnitude (average $^{10}Be/^{9}Be=1.67\times10^{-15}$). Data for procedural blanks and their corresponding sample sets are shown in Table DR1. A known quantity of ^{9}Be carrier was added to facilitate AMS analysis of the small $^{10}Be/^{9}Be$ ratios in each sample. Blanks BL7 and BL8 received a known concentration of a commercial ^{9}Be carrier (1000 μg ^{9}Be/ml) whereas B6 received known concentration of the Merck carrier (1000 μg ^{9}Be/ml). Carrier addition to associated samples was adjusted based on sample weight. The sample sets corresponding to blanks B8 and B9 each received 1.0 ml of the OSU Blue carrier (240±3 μg ^{9}Be/ml), regardless of sample mass. The $^{10}Be/^{9}Be$ ratio for this carrier is $\sim 4\times10^{-16}$. All laboratory-based chemical data are summarized in Table DR1.

The pure sample quartz with carrier was then fully dissolved in concentrated HF over mild heat. Following several treatments of oxidization via $HClO_4$, all samples were passed through anion and cation exchange columns to remove elemental impurities (e.g., Fe, Ti, Al). This was followed by a series of pH-sensitive selective chemical precipitations and pH-8 water rinsing for boron isobar removal, resulting finally in a pure beryllium hydroxide precipitate. The $Be(OH)_2$ was transferred to a quartz vial for high-temperature dry-down and oxidation to BeO, which was finally mixed with a powdered niobium binder and loaded into the AMS target vessel by compaction. The samples were sent to Purdue University's Rare Isotope Measurement Laboratory (PRIME-Lab) for AMS measurement of the $^{10}Be/^{9}Be$ ratios (Table DR1).

Production Rate Calculation and Scaling

The online CRONUS-Earth calculator (http://hess.ess.washington.edu/math) has traditionally used only production rates derived from a globally distributed set of calibration data sites (Balco et al., 2008). Regional production rates, however, have recently been developed. We utilize a production rate calibrated to the southern mid-latitudes of New Zealand (Putnam et al., 2010), derived by matching the cosmogenic ^{10}Be concentrations in boulders from a debris flow deposit with radiocarbon-dated macrofossils of shrub-like vegetation from a soil horizon directly underneath the deposit. The reference ^{10}Be production rate=3.75±0.08 atoms g^{-1} yr^{-1}, with a scaling error of <2.5% (Putnam et al., 2010; Balco et al., 2009). Justification for applying this reference production rate to southern Patagonia is based upon comparison between maximum- and minimum-limiting ^{14}C ages and ^{10}Be boulder concentration measurements both from the Puerto Banderas moraine near Lago Argentino (Fig. DR1) (Ackert et al., 2008; Kaplan et al., 2011). The original ^{14}C dates indicate moraine deposition after 12.9±0.9 ka and before ~12.3 ka (Strelin and Malignino, 2000). More recent ^{14}C dating tightly constrains the moraine age to ~13 ka with retreat before ~12.7 ka (Strelin et al., 2011). By using the New Zealand production rate from Putnam et al. (2010), the ^{10}Be boulder samples from the moraine of Ackert et al. (2008)

date to 13.2±0.3 ka, in agreement with the ^{14}C constraints (Strelin et al., 2011). This agreement between the radiocarbon data and the cosmogenic radionuclide measurements for the Puerto Banderas moraine is maintained only by using the production rate established by Putnam et al. (2010). The globally-averaged production rate calculator (Balco et al., 2008) results in a significantly younger age of 11.4±0.3 ka that contradicts the ^{14}C age constraints. Kaplan et al. (2011) obtained additional ^{10}Be dates from the Puerto Banderas Moraine and on an in-board ^{14}C-dated moraine that confirmed the applicability of this production rate to southern Patagonia.

Our cosmogenic ^{10}Be concentrations and all relevant sample data (Table DR1) were entered into the online CRONUS-Earth online surface exposure age calculator. The results from both calculators described above are shown for comparison in Table DR2. Age results from all five scaling schemes (St: Lal (1991) and Stone (2000); De: Desilets et al. (2006); Du: Dunai (2001); Li: Lifton et al. (2005); and Lm: Lal (1991) and Stone (2000), time-dependent scheme) are also provided (Table DR3). Our interpretations reference the ages calculated with the Lm scaling scheme. The use of any one scaling scheme does not significantly affect the calculated ages or conclusions.

Exposure Age Results

Glacial retreat timing for each moraine was established by calculating the mean of each sample set, expressed with one standard error (S.E.) uncertainty (Figs. 1 and 2 in the main text). We use the straight mean because the geologic uncertainty (standard deviation of the boulder ages for each moraine) is equivalent to or greater than the analytical uncertainty of individual boulders (Bevington and Robinson, 2002). Using a weighted mean does not change our results or conclusions. The La Sofia moraine has an exposure age of 19.7±1.1 ka (n=6; mean standard weighted deviates (MSWD)=4.5) whereas the adjacent San Jorge moraine 1.5 km upstream has an exposure age of 18.9±0.4 ka (n=9; MSWD=1.4). The Cerro Pintado moraine has an error-weighted mean age of 17.0±0.3 ka (n=6; MSWD=0.88). No outliers were excluded from the age calculations. Our Rio Guanaco Valley ^{10}Be retreat chronology is older than the minimum-limiting ^{14}C dates that show the San Jorge and Cerro Pintado moraines to be older than 13.7±0.1 ka and 4.8±0.2 ka, respectively (Wenzens, 1999). The relevant field and laboratory data needed to re-calculate the surface exposure ages are provided in Table DR1. Interpretations are discussed in the main text.

Paleo-ELA Calculation

Estimates for the paleo-equilibrium line altitude (ELA) values were approximated via inferred paleo-glacier extents and moraine landscape positions. The glacial extents were estimated by constraining the area of glacial presence to areas upstream of the respective terminal moraines, and then confining the estimated location of glacial margins inside the valley walls, with the upper accumulation zone filling the headwalls (Fig. 1). The paleo-glacial surface elevations were interpolated at each point across the valley by matching identical glacier margin elevation values derived from a digital elevation model (DEM) dataset. A smoothed surface approximating the paleo-glacier surface was constructed using the ESRI© ArcMap program. Glacier surface elevations were plotted in hypsometric curves versus the cumulative area below each elevation value. The elevation corresponding to the accumulation area ratio of 0.65±0.05

(Porter, 1975) (elevation with 35% of glacial area below the ELA) was used as an approximation of the paleo-ELA. Paleo-ELAs were converted into past temperature conditions by using a lapse rate of 0.008 °C m^{-1} (Hulton et al., 1994; Takeuchi et al., 1996; Stuefer et al., 2007). In order to tie the paleo-ELA estimates to modern conditions, we calculated the averaged present-day ELA value from a set of 12 existing cirque glaciers positioned on the crest of the pre-Cordilleran mountain range west of Rio Guanaco Valley (Fig. 1b); this present-day ELA value is estimated to be 1750±200 m (one standard deviation uncertainty), and was also computed via the AAR method. The paleo-ELA results corresponding to conditions during each respective moraine deposition are discussed in the main text.

Climate Model Simulations for 50°S

We use the climate output for 50°S, southern Patangonia from a fully-coupled atmosphere-ocean global circulation model (AOGCM) to calculate deglacial changes in ELA from the LGM (Fig. 3d). The National Center for Atmospheric Research (NCAR) CCSM3 model simulation starts from an equilibrium LGM state that incorporates orbital variations, known greenhouse gas concentrations (Joos and Spahni, 2008), and ice sheet size (Liu et al., 2009). The AOGCM was run 22 to 14 ka with perturbation by a varying meltwater flux from the melting Northern Hemisphere ice sheets discharged into the North Atlantic Ocean 19–17 ka (Liu et al., 2009). This results in surface cooling in the North Atlantic with simultaneous warming in the southern mid to high-latitudes, consistent with a bipolar thermal seesaw teleconnection between the Northern and Southern Hemispheres related to reduced meridional overturning in the North Atlantic (Crowley, 1992; Stocker, 1998). The modeled range of temperature change across southern South America from 19 to 17 ka is 1–3°C, a warming that is explained solely by the meltwater flux into the North Atlantic because atmospheric greenhouse gas forcings were not initiated until 17 ka (Liu et al., 2009), in agreement with most recent greenhouse gas chronology (Lemieux-Dudon et al., 2010).

The transient AOGCM climate for Patagonia, 50°S, was converted to a relative change in ELA due to austral summer temperatures (December through February) by using the temperature lapse rate of 0.008 °C m^{-1} (Hulton et al., 1994; Takeuchi et al., 1996; Stuefer et al., 2007), as well as ELA change due to precipitation (-0.0083 mm day^{-1} m^{-1}) based on the Southern Patagonian Icefield modeling of Hulton et al. (1994) (Fig. 3d). This modeled change in ELA is an estimate made relative to a zero value established from the 2 kyr average of relatively constant glacial-state conditions from 22–20 ka. We also compared our ELA changes with predicted ELA changes from a transient CCSM3 simulation run from 22 to 17 ka but with only changes in orbital parameters to test the effects of spring-summer insolation (Stott et al., 2007).

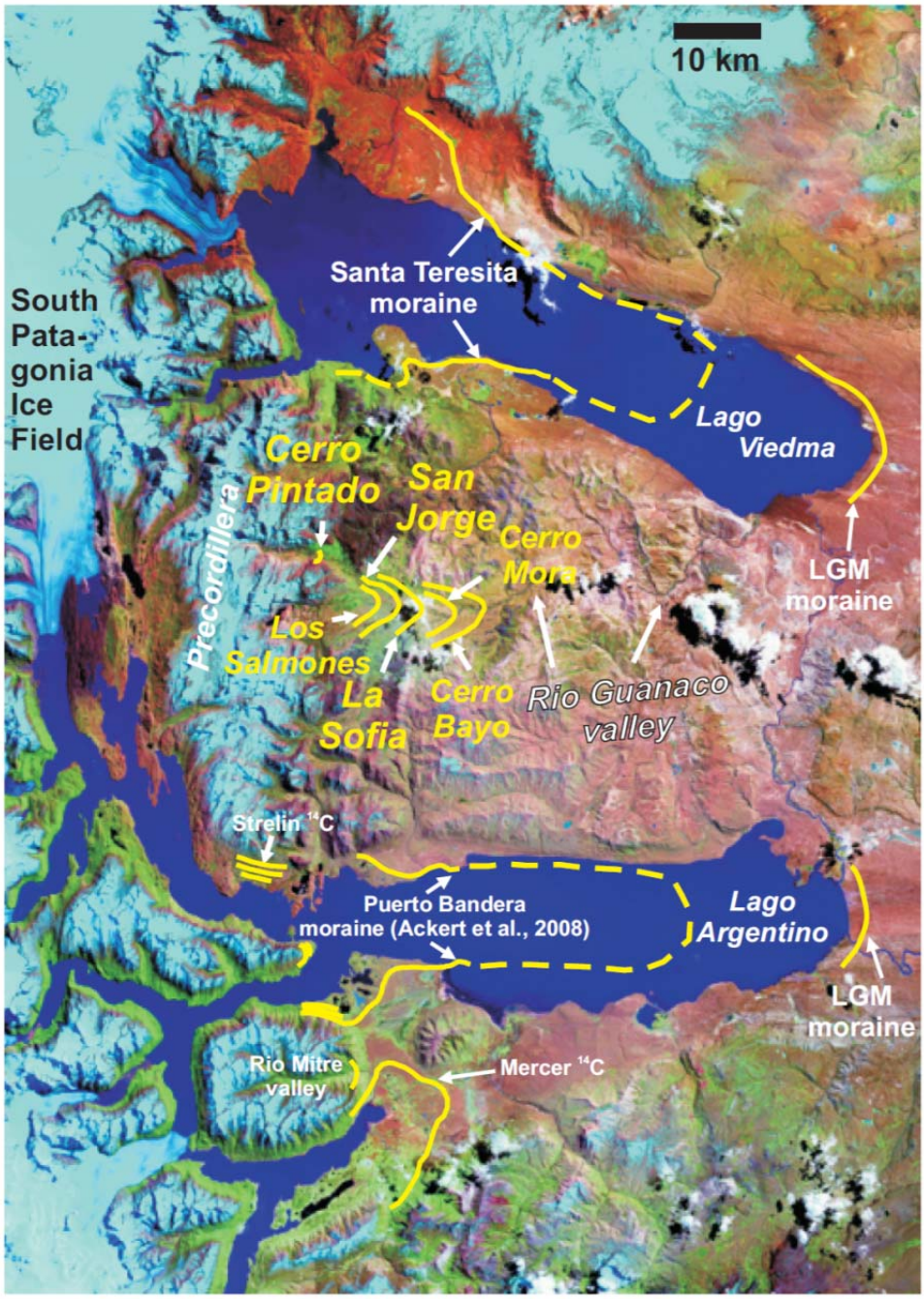

Figure DR1: Map of the Rio Guanaco Valley study area. LANDSAT Image showing known moraine features are shown with solid yellow lines; inferred moraine locations are shown by dashed lines (Wenzens, 1999).

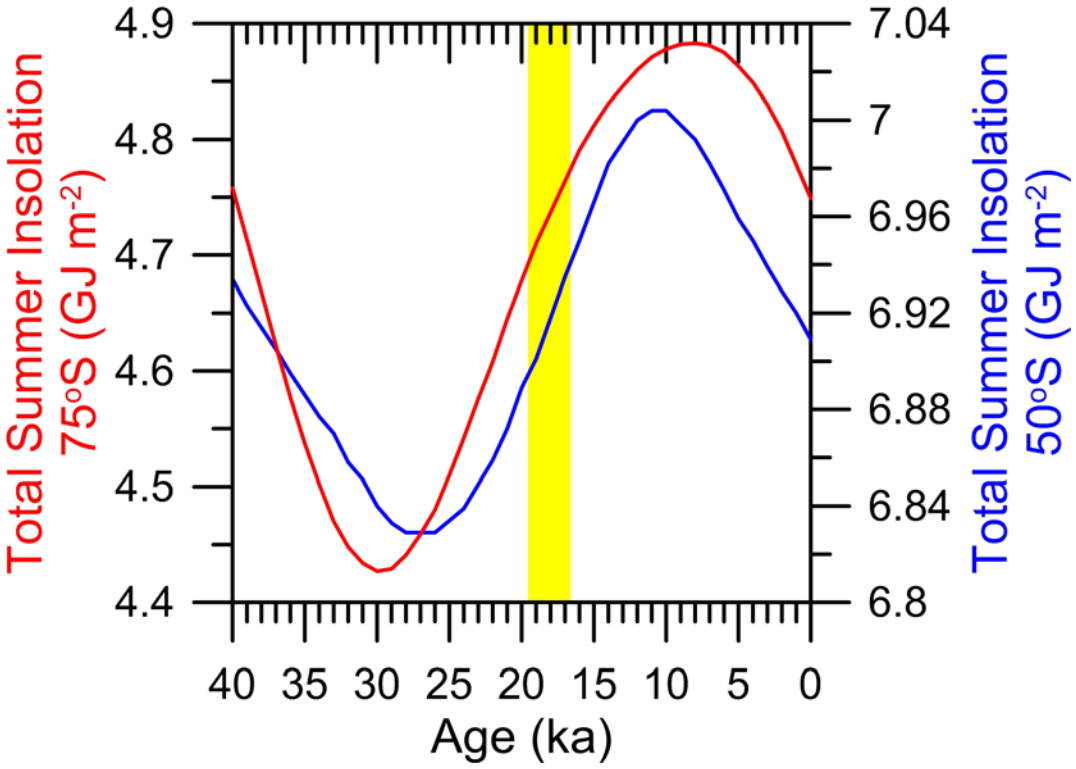

Figure DR2: Changes in total austral summer length as a reflection of summer duration with a cut off of 250 W m^{-2} (Huybers and Denton, 2008). Red is for 75°S, blue for 50°S. Yellow bar denotes the retreat of ice in Rio Guanaco Valley.

Figure DR3: View along crest of La Sofia moraine, facing north.

Figure DR4: Representative boulder (RGV-10-20) from the crest of the La Sofia moraine in Rio Guanaco Valley.

Figure DR5: View of the southern flank of the San Jorge moraine arc as it spans the Rio Guanaco Valley, facing north-northwest. Moraine feature spans the center portion of the photograph. The mouth of Rio Manga Norte Valley as it enters into Rio Guanaco Valley is seen in the center background.

Figure DR6: View of San Jorge moraine crest, arcing to the left from foreground to background, facing north-northeast.

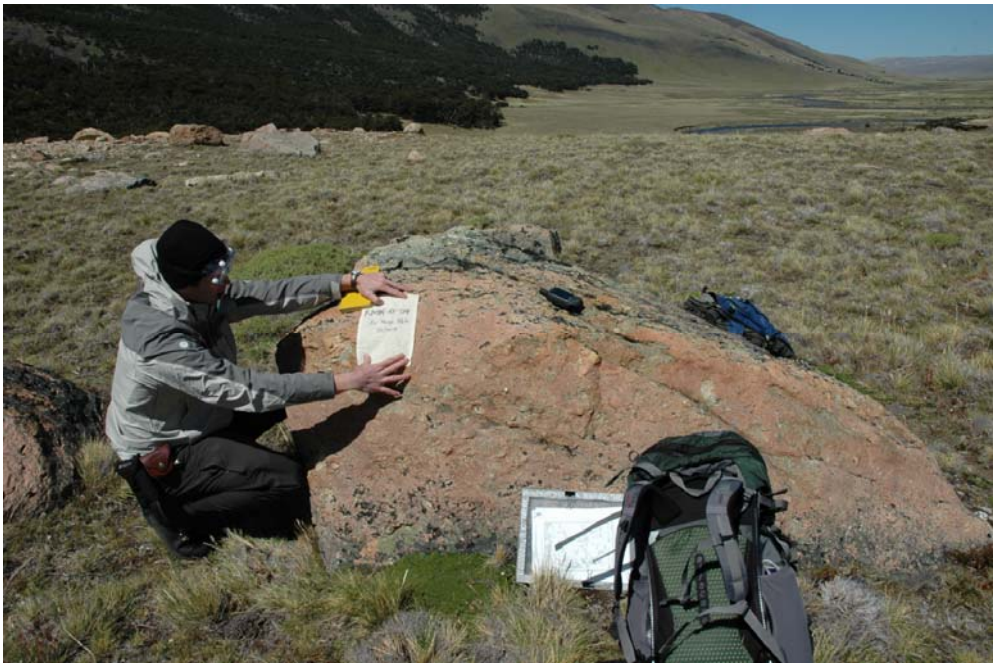

Figure DR7: Representative sample boulder (RMN-10-04) from the Cerro Pintado moraine in Rio Manga Norte Valley.

Figure DR8: View of Cerro Pintado moraine and representative boulder sample, facing south-southeast. Note the moraine spans nearly the entire valley, and is incised by the Rio Manga Norte. Downstream (left) leads to the main Rio Guanaco Valley.

Supplementary Figure DR9: View of Cerro Pintado moraine (Rio Manga Norte Valley) facing north-northeast.

Supplementary Table DR1: Field and laboratory data for ^{10}Be surface exposure age calculations

Sample ID	Latitude (°S)	Long. (°W)	Elev. (m)	Height (cm)	Sample thickness (cm)	Lith.	Qtz. (%)	Mass of quartz (g)	Shielding factor	^{10}Be standard[a]	Blank	^{10}Be conc. (10^4)	^{10}Be uncertainty (10^3)
La Sofia													
RGV-10-10	49.925	72.719	774	240	2	Rhyolite	10-15	21.543	0.999996	07KNSTD	B8	14.12	8.00
RGV-10-16	49.919	72.701	656	110	1.9	Rhyolite	5-10	20.479	0.999746	07KNSTD	B9	14.82	8.10
RGV-10-18	49.920	72.704	700	250	1.5	Rhyolite	5-10	21.541	0.999877	07KNSTD	B8	13.71	6.38
RGV-10-20	49.921	72.707	720	300	1	Rhyolite	10	20.991	0.999879	07KNSTD	B8	16.42	10.7
RGV-10-21	49.922	72.708	733	60	1.2	Rhyolite	5-10	20.558	0.999879	07KNSTD	B8	14.17	8.35
RGV-10-22	49.924	72.714	767	150	1.4	Rhyolite	15	23.589	0.999996	07KNSTD	B8	18.92	9.55
San Jorge													
RGV-04-01	49.913	72.728	672	145	2	Rhyolite	15-20	32.7248	0.999797	KNSTD	BL8	15.76	10.1
RGV-04-03	49.914	72.728	680	177	2.5	Rhyolite	15-20	38.9325	0.999842	NIST_30600	BL7	15.39	9.17
RGV-04-04A	49.914	72.720	671	140	3	Rhyolite	20	38.5150	0.999803	NIST_30600	BL7	15.12	11.0
RGV-04-05	49.917	72.730	690	95	2.5	Rhyolite	15	39.2948	0.999789	NIST_30600	BL7	16.62	9.14
RGV-04-07	49.917	72.721	698	2.0	2	Rhyolite	10-15	30.7075	0.999748	NIST_30600	BL7	15.13	23.1
RGV-04-02	49.914	72.720	670	3.5	3	Rhyolite	10	40.010	0.9998	07KNSTD	B6	14.80	10.5
RGV-04-06	49.914	72.720	678	85	2	Rhyolite	10-15	40.336	0.999834	07KNSTD	B6	13.43	6.65
RGV-04-08	49.917	72.721	693	100	2.5	Rhyolite	10-15	40.164	0.99974	07KNSTD	B6	12.28	7.23
RGV-04-09	49.916	72.722	691	83	3	Rhyolite	10	40.145	0.99972	07KNSTD	B6	14.43	7.24
Cerro Pintado													
RMN-10-01	49.857	72.837	758	150	1.5	Rhyolite	10	30.530	0.994347	07KNSTD	B8	13.22	5.11
RMN-10-04	49.85	72.835	765	100	2.5	Rhyolite	10	30.321	0.992884	07KNSTD	B8	13.46	5.15
RMN-10-05	49.858	72.835	776	250	2.6	Rhyolite	10-15	30.245	0.989931	07KNSTD	B8	13.73	6.96
RMN-10-06	49.859	72.834	754	150	2	Rhyolite	10	30.750	0.989931	07KNSTD	B9	12.93	7.10
RMN-10-07	49.859	72.834	750	200	2.3	Rhyolite	10-15	30.872	0.99509	07KNSTD	B9	13.06	5.36
RMN-10-08	49.861	72.832	742	300	1.3	Rhyolite	10-15	30.387	0.992027	07KNSTD	B9	14.34	5.69

	Blank ^{10}Be/^{9}Be	Error		
Blank BL7	2.64 E-14	3.88 E-15		
Blank BL8	2.64 E-14	4.70 E-15		
Blank B6	**2.89 E-15**	**0.95 E-15**		
Blank B8	**0.86 E-15**	**1.22 E-15**		
Blank B9	**1.25 E-15**	**1.08 E-15**	**Range (B6-B9) = 2.03 E-15**	**Average (B6-B9) = 1.67 E-15**

[a]All samples underwent accelerator mass spectrometric analysis of the ^{10}Be/^{9}Be ratios at Purdue's Rare Isotope Measurement laboratory (PRIME-Lab) according to the following AMS beryllium standardizations, as noted: NIST_30600 (NIST SRM4325 with an assumed isotope ratio of 3.0×10^{-11}), KNSTD, and 07KNSTD.

Table DR2: Comparison of calculated surface exposure ages according to ^{10}Be reference production rate calculator and erosion rate.

	Global production rate[a] Zero erosion		**Global production rate Erosion = 1.4 mm/k.y.[c]**		**SH production rate[b] Zero erosion**		**SH production rate Erosion = 1.4 mm/k.y.**	
La Sofia moraine	Age	Uncertainty[c] (1 std-error)	Age	Uncertainty (1 std-error)	Age	Uncertainty (1 std-error)	Age	Uncertainty (1 std-error)
RGV-10-10	14664	813	14913	841	17069	948	17406	986
RGV-10-16	16999	912	17334	949	19789	1063	20244	1113
RGV-10-18	15099	689	15363	713	17575	803	17932	836
RGV-10-20	17694	1130	18058	1177	20602	1318	21097	1382
RGV-10-21	15141	874	15406	905	17624	1019	17984	1061
RGV-10-22	19641	974	20092	1019	22871	1136	23482	1198
n = 6	16.5 ± 0.9	MSWD = 4.5	16.9 ± 0.9	MSWD = 4.5	19.3 ± 1.0	MSWD = 4.5	**19.7 ± 1.1 ka (1 std-error)**	**MSWD = 4.5**
San Jorge moraine	Age	Uncertainty (1 std-error)	Age	Uncertainty (1 std-error)	Age	Uncertainty (1 std-error)	Age	Uncertainty (1 std-error)
RGV-04-01	16295	1024	16603	1063	18968	1194	19386	1247
RGV-04-03	16035	937	16333	972	18665	1092	19069	1140
RGV-04-04A	15779	1125	16067	1167	18366	1312	18757	1368
RGV-04-05	17237	930	17582	968	20067	1084	20536	1136
RGV-04-07	15556	2328	15836	2412	18107	2713	18487	2828
RGV-04-02	16926	1178	17258	1225	19704	1373	20155	1437
RGV-04-06	15139	734	15404	760	17620	856	17979	891
RGV-04-08	13727	791	13944	816	15977	922	16271	956
RGV-04-09	16211	798	16516	828	18871	930	19284	971
n = 9	15.9 ± 0.4	MSWD = 1.4	16.2 ± 0.4	MSWD = 1.4	18.5 ± 1.4	MSWS = 1.4	**18.9 ± 0.4 ka (1 std-error)**	**MSWD = 1.4**
Cerro Pintado moraine	Age	Uncertainty (1 std-error)	Age	Uncertainty (1 std-error)	Age	Uncertainty (1 std-error)	Age	Uncertainty (1 std-error)
RMN-10-01	13948	528	14172	545	16235	615	16539	638
RMN-10-04	14251	534	14486	552	16588	623	16905	647
RMN-10-05	14455	718	14697	742	16825	837	17152	869
RMN-10-06	13803	743	14023	766	16066	866	16364	898
RMN-10-07	13956	561	14181	579	16244	654	16548	679
RMN-10-08	15347	597	15619	618	17863	696	18233	725
n = 6	14.3 ± 0.3	MSWD = 0.88	14.5 ± 0.3	MSWD = 0.88	16.6 ± 0.3	MSWD = 0.88	**17.0 ± 0.3 ka (1 std-error)**	**MSWD = 0.88**

[a]Global production rate refers to the conventional global production rate calculator from Balco et al.(2008); [b]SH production rate refers to the reference production rate established for the southern mid-latitudes of New Zealand by Putnam et al.(2010); [c]erosion rate is assumed to equal 1.4 mm/k.y. (Douglass et al., 2006). All ages were calculated with the online CRONUS-Earth surface exposure age calculator using the time-dependent Lal (1991)/Stone (2000) scaling scheme results (Lm). Individual exposure age outputs from the CRONUS Earth online calculator are expressed with one standard-error uncertainty. Final inverse-variance weighted-average ages are also shown with one standard-error uncertainty. [c]All input errors represent the internal uncertainty of each sample (one standard-error).

Table DR3: Surface exposure age results and cosmogenic radionuclide scaling schemes.

	Lal/Stone[a]		Desilets et al.[b]		Dunai[c]		Lifton et al.[d]		L/S time-dependent[e]	
La Sofia moraine	Age	Uncertainty[f] (1 std-error)	Age	Uncertainty (1 std-error)	Age	Uncertainty (1 std-error)	Age	Uncertainty (1 std-error)	Age	Uncertainty (1 std-error)
RGV-10-10	16996	986	17652	986	17838	986	17474	986	17406	986
RGV-10-16	19784	1113	20561	1113	20798	1113	20346	1113	20244	1113
RGV-10-18	17512	836	18209	836	18408	836	18033	836	17932	836
RGV-10-20	20626	1382	21400	1382	21644	1382	21150	1382	21097	1382
RGV-10-21	17564	1061	18251	1061	18448	1061	18067	1061	17984	1061
RGV-10-22	22981	1198	23790	1198	24060	1198	23461	1198	23482	1198
	19.2 ± 1.0	MSWD = 4.4	20.0 ± 1.1	MSWD = 4.6	20.2 ± 1.1	MSWD = 4.7	19.8 ± 1.0	MSWD = 4.4	**19.7 ± 1.1 ka (1 std-error)**	**MSWD = 4.5**
San Jorge moraine	Age	Uncertainty (1 std-error)	Age	Uncertainty (1 std-error)	Age	Uncertainty (1 std-error)	Age	Uncertainty (1 std-error)	Age	Uncertainty (1 std-error)
RGV-04-01	18940	1247	19691	1247	19915	1247	19494	1247	19386	1247
RGV-04-03	18630	1140	19369	1140	19587	1140	19177	1140	19069	1140
RGV-04-04A	18323	1368	19052	1368	19265	1368	18866	1368	18757	1368
RGV-04-05	20072	1136	20850	1136	21090	1136	20625	1136	20536	1136
RGV-04-07	18057	2828	18777	2828	18985	2828	18594	2828	18487	2828
RGV-04-02	19698	1437	20466	1437	20701	1437	20250	1437	20155	1437
RGV-04-06	17558	891	18264	891	18465	891	18092	891	17979	891
RGV-04-08	15878	956	16532	956	16707	956	16394	956	16271	956
RGV-04-09	18842	971	19579	971	19798	971	19377	971	19284	971
	18.4 ± 0.4	MSWD = 1.4	19.2 ± 0.4	MSWD = 1.5	19.4 ± 0.5	MSWD = 1.5	19.0 ± 0.4	MSWD = 1.4	**18.9 ± 0.4 ka (1 std-error)**	**MSWD = 1.4**
Cerro Pintado moraine	Age	Uncertainty (1 std-error)	Age	Uncertainty (1 std-error)	Age	Uncertainty (1 std-error)	Age	Uncertainty (1 std-error)	Age	Uncertainty (1 std-error)
RMN-10-01	16149	638	16783	638	16956	638	16631	638	16539	638
RMN-10-04	16511	647	17151	647	17329	647	16989	647	16905	647
RMN-10-05	16754	869	17396	869	17577	869	17227	869	17152	869
RMN-10-06	15976	898	16608	898	16779	898	16460	898	16364	898
RMN-10-07	16158	679	16795	679	16969	679	16644	679	16548	679
RMN-10-08	17817	725	18500	725	18700	725	18313	725	18233	725
	16.6 ± 0.3	MSWD = 0.85	17.2 ± 0.3	MSWD = 0.90	17.4 ± 0.3	MSWD = 0.93	17.0 ± 0.3	MSWD = 0.86	**17.0 ± 0.3 ka (1 std-error)**	**MSWD = 0.88**

[a]Constant rate Lal (1991) and Stone (2000) scheme; [b]Desilets et al. (2006); [c]Dunai (2001); [d]Lifton et al. (2005); [e]modified Lal (1991)/Stone (2000) scaling scheme based on time-dependent magnetic field variations Nishiizumi et al. (1989), used in this study. [f]Input errors represent internal sample uncertainties (1 std-error). The final inverse variance weighted-average ages are also displayed with one standard-error uncertainty.

Supplementary References

Ackert, R.P., Becker, R.A., Singer, B.S., Kurz, M.D., Caffee, M.W., and Mickelson, D.M., 2008, Patagonian glacier response during the Late Glacial-Holocene transition: Science, v. 321, p. 392-395.

Balco, G., Stone, J.O., Lifton, N.A., and Dunai, T.J., 2008, A complete and easily accessible means of calculating surface exposure ages or erosion rate from ^{10}Be and ^{26}Al measurements: Quaternary Geochronology, v. 3, p. 174-195.

Balco, G., Briner, J., Finkel, R.C., Rayburn, J.A., Ridge, J.C., and Schaefer, J.M., 2009, Regional beryllium-10 production rate calibration for late-glacial northeastern North America: Quaternary Geochronology, v. 4, p. 93-107.

Balco, G., 2011, Contributions and unrealized potential contributions of cosmogenic-nuclide exposure dating to glacier chronology, 1990-2010: Quaternary Science Reviews, v. 30, p. 3-27.

Bevington, P., and Robinson, D.K., 2002, Data Reduction and Error Analysis for the Physical Sciences, 3rd ed.: McGraw-Hill, Boston, 336 pp.

Caldenius, C., 1932, Las glaciaciones Cuaternarias en la Patagonia y Tierra del Fuego: Geografiska Annaler, v. 14, p. 1-164.

Crowley, T., 1992, North Atlantic Deep Water cools the Southern Hemisphere: Paleoceanography, v. 7, p. 489-497.

Desilets, D., Zreda, M., and Prabu, T., 2006, Extended scaling factors for in situ cosmogenic nuclides: New measurements at low latitude: Earth and Planetary Science Letters, v. 246, p. 265-276.

Douglass, D.C., Singer, B.S., Kaplan, M.R., Mickelson, D.M., and Caffee, M.W., 2006, Cosmogenic nuclide surface exposure dating of boulders on last-glacial and late-glacial moraines, Lago Buenos Aires, Argentina: Interpretive strategies and paleoclimate implications: Quaternary Geochronology, v. 1, p. 43-58.

Dunai, T., 2001, Influence of secular variation of the magnetic field on production rates of in situ produced cosmogenic nuclides: Earth and Planetary Science Letters, v. 193, 197-212.

Gosse, J.C., and Phillips, F.M., 2001, Terrestrial in situ cosmogenic nuclides: theory and application: Quaternary Science Reviews, v. 20, p. 1475-1560.

Hulton, N., Sugden, D., Payne, A., and Clapperton, C., 1994, Glacier modeling and the climate of Patagonia during the Last Glacial Maximum: Quaternary Research, v. 42, p. 1-19.

Huybers, P., and Denton, G., 2008, Antarctic temperature at orbital timescales controlled by local summer duration: Nature Geoscience, v. 1, p. 787-792.

Joos, F., and Spahni, R., 2008, Rates of change in natural and anthropogenic radiative forcing over the past 20,000 years: Proceedings of the National Academy of Sciences, v. 105, p. 1425-1430.

Kaplan, M.R., Strelin, J.A., Schaefer, J.M., Denton, G.H., Finkel, R.C., Schwartz, R., Putnam, A.E., Vandergoes, M.J., Goehring, B.M., and Travis, S.G., 2011, In-situ cosmogenic ^{10}Be production rate at Lago Argentino, Patagonia: Implications for late-glacial climate chronology: Earth and Planetary Science Letters, v. 309, p. 21-32.

Lal, D., 1991, Cosmic ray labeling of erosin surfaces: in situ nuclide production rates and erosion models: Earth and Planetary Science Letters, v. 104, p. 424-439.

Lemieux-Dudon, B., Blayo, E., Petit, J., Waelbroeck, C., Svensson, A., Ritz, C., Barnola, J., Narcisi, B.M., and Parrenin, F., 2010, Consistent dating for Antarctic and Greenland ice cores: Quaternary Science Reviews, v. 29, p. 8-20.

Lifton, N., Bieber, J., Clem, J., Duldig, M., Evenson, P., Humble, J., and Pyle, R., 2005, Addressing solar modulation and long-term uncertainties in scaling secondary cosmic rays for in situ cosmogenic nuclide applications: Earth and Planetary Science Letters, v. 239, p. 140-161.

Liu, Z., Otto-Bliesner, B.L., He., F., Brady, E.C., Tomas, R., Clark, P.U., Carlson, A.E., Lynch-Stieglitz, J., Curry, W., Brook, E., Erickson, D., Jacob, R., Kutzbach, J., and Cheng, J., 2009, Transient simulation of last deglaciation with a new mechanism for Bølling-Allerød warming: Science, v. 325, p. 310-314.

Mercer, J.H., 1976, Glacial history of southernmost South America: Quaternary Research, v. 6, p. 125-166.

Nishiizumi, K., Winterer, E., Kohl, C., Klein, J., Middleton, R., Lal, D., and Arnold, J., 1989, Cosmic ray production rates of ^{26}Al and ^{10}Be in quartz from glacially polished rocks: Journal of Geophysical Research, v. 94, v. 17,907-17,915.

Porter, S. C., 1975, Equilibrium-line altitudes of late Quaternary glaciers in the Southern Alps, New Zealand: Quaternary Research, v. 5, p. 27-47.

Putnam, A.E., Schaefer, J.M., Barrell, D.J.A., Vandergoes, M., Denton, G.H., Kaplan, M.R., Finkel, R.C., Schwartz, R., Goehring, B.M., and Kelley, S.E., 2010, *In situ* cosmogenic ^{10}Be production-rate calibration from the Southern Alps, New Zealand: Quaternary Geochronology, v. 5, p. 392-409.

Stocker, T. F., 1998, The seesaw effect: Science, v. 281, 61-62.

Stone, J. O., 2000, Air pressure and cosmogenic isotope production: Journal of Geophysical Research, v. 105, p. 23753-23759.

Stott, L., Timmermann, A., and Thunell, R., 2007, Southern Hemisphere and Deep-Sea Warming Led Deglacial Atmospheric CO2 Rise and Tropical Warming: Science, v. 318, p. 435-438.

Strelin, J.A., and Malignino, E.C., 2000, Late-glacial history of Lago Argentino, Argentina, and age of the Puerto Bandera moraines: Quaternary Research, v. 54, p. 339-347.

Strelin, J.A., Denton, G.H., Vandergoes, M.J., Ninnemann, U.S., and Putnam, A.E., 2011, Radiocarbon chronology of the late-glacial Puerto Bandera moraines, Southern Patagonian Icefield, Argentina: Quaternary Science Reviews, v. 30, p. 2551-2569.

Stuefer, M., Rott, H., and Skvarca, P., 2007, Glacier Perito Moreno, Patagonia: climate sensitivities and glacier characteristics preceding the 2003/04 and 2005/06 damming events: Journal of Glaciology, v. 53, p. 3-16.

Takeuchi, Y., Naruse, R., and Skvarca, P., 1996, Annual air-temperature measurement and ablation estimate at Moreno Glacier, Patagonia: Bulletin of Glacier Research, v. 14, p. 23-28.

Wenzens, G., 1999, Fluctuations of outlet and valley glaciers in the southern Andes (Argentina) during the past 13,000 years: Quaternary Research, v. 51, p. 238-247.